Available online at www.sciencedirect.com
ScienceDirect
International Journal of Heat and Mass Transfer 49 (2006) 4850–4866
International Journal of HEAT and MASS TRANSFER
www.elsevier.com/locate/ijhmt

Control of macrosegregation during the solidification of alloys using magnetic fields

Deep Samanta, Nicholas Zabaras *

Materials Process Design and Control Laboratory, Sibley School of Mechanical and Aerospace Engineering, 188 Frank H.T. Rhodes Hall, Cornell University, Ithaca, NY 14853-3801, USA

Received 28 September 2005
Available online 1 September 2006

Abstract

Numerical modeling of convection damping and macrosegregation suppression during solidification of alloys with prominent mushy zones through the use of tailored magnetic fields is demonstrated here. Macrosegregation leads to commonly observed defects such as freckles, channels and segregates in cast alloys that severely affect the performance and suitability of the alloy for further applications. The current work demonstrates the successful use of magnetic fields in suppressing thermosolutal convection and eliminating some of these defects in solidifying metallic alloys. The computational model presented utilizes volume-averaged governing transport equations and stabilized finite element techniques to discretize these equations. A finite-dimensional optimization problem, based on the continuum sensitivity method is considered to design the time history of the imposed magnetic field required to effectively damp convection. The coefficients that determine this time variation are the main design parameters of this optimization problem. Continuum sensitivity equations are derived by design-differentiating the governing equations of the direct problem. The cost functional here is given by the square of the L_2 norm of an expression representing the deviation of the volume-averaged velocity corresponding to conditions of convection less growth. The cost functional minimization process is realized through a non-linear conjugate gradient algorithm that utilizes finite element solutions of the continuum direct and sensitivity problems. Design of the time history of the imposed magnetic field is highlighted through different examples with the main objective being the suppression of convection and macrosegregation during alloy solidification.

Keywords: Convection damping; Optimal magnetic field; Macrosegregation; Lorentz force; Continuum sensitivity method; Optimization; Design

1. Introduction

Solidification of most alloys often results in macrosegregation or large scale variations in the concentration of solute elements. Macrosegregation leads to non-uniform properties in the alloy that severely deteriorate its performance and suitability in many applications. In metallic cast alloys, macrosegregation manifests itself for example in the form of defects such as freckles, channels, bleed bands, centerline segregates and A- and V-segregates. Removal of most of these defects either leads to significant material and monetary losses or render the casting unusable for further applications. In the aircraft industry for example, almost 40% of the directionally solidified single crystal blades are lost during castings. Thermosolutal buoyancy forces are the primary cause of macrosegregation in alloys solidifying in terrestrial gravity conditions. These forces may be supplemented by thermocapillary or diffusocapillary forces, if surface tension effects are significant, and shrinkage driven flows. Damping thermosolutal convection is indispensable for suppressing and minimizing macrosegregation in cast alloys.

The role of thermosolutal convection in macrosegregation has been highlighted through experiments and

* Corresponding author. Tel.: +1 607 255 9104; fax: +1 607 255 1222.
E-mail address: zabaras@cornell.edu (N. Zabaras).
URL: http://mpdc.mae.cornell.edu/ (N. Zabaras).

0017-9310/$ - see front matter © 2006 Elsevier Ltd. All rights reserved.
doi:10.1016/j.ijheatmasstransfer.2006.05.045

Nomenclature

da	interfacial area
B	magnitude of magnetic field
$\mathbf{B}$	magnetic field
ΔB	perturbation in B
$\{b\}$	design parameters
$\mathscr{B}$	Bezier–Bernstein polynomial
C	solute concentration
ΔC	difference in maximum and minimum solute concentration
c_p	specific heat
c_p^*	average specific heat
$\overset{\circ}{C}$	sensitivity solute concentration
$\overset{\circ}{C}_\mathrm{l}$	sensitivity liquid solute concentration
d	dendrite arm spacing
D	solute diffusivity
$\mathbf{e}$	direction cosines
$\mathbf{E}$	induced electric field
f	mass fraction
$\mathbf{F}$	Gradient of cost functional
$\mathscr{F}$	mushy zone factor
g	gravity constant
G	vertical thermal gradient
h	enthalpy, convection heat transfer coefficient
H	height
I	flux term from volume averaging
$\mathbf{J}$	electric current density
J	cost functional
K	permeability
k	thermal conductivity
L	length, characteristic length
m	slope of phase diagram lines
M	sensitivity matrix
$\mathbf{n}$	normal vector
N	size of the design space
p	pressure
$\overset{\circ}{p}$	sensitivity pressure
r	bottom cooling rate
Ra	Rayleigh number
$\underline{\mathbf{S}}$	velocity gradients with respect to design variables
$\mathbf{S}$	individual vectors in $\underline{\mathbf{S}}$
t	time
$\hat{t}$	non-dimensional time
T	temperature
$\overset{\circ}{T}$	sensitivity temperature
dV	averaging volume
v	velocity magnitude
$\boldsymbol{v}$	volume-averaged velocity
$\overset{\circ}{\boldsymbol{v}}$	sensitivity velocity
W	width
x	x coordinate
$\boldsymbol{x}$	vector in space
$\mathbf{Y}$	field variable
$\overset{\circ}{\mathbf{Y}}$	sensitivity of field variable
y	y coordinate
z	z coordinate

Greek symbols

α	step size in CG algorithm
β	coefficient of expansion
ϵ	liquid volume fraction
$\overset{\circ}{\epsilon}$	sensitivity liquid volume fraction
κ_p	partition coefficient
μ	liquid viscosity
Ω	physical domain
ϕ	electric potential
$\overset{\circ}{\phi}$	sensitivity electric potential
ρ	density
ρ_e	charge density
σ_e	electrical conductivity

Subscripts

C	solutal
conv	convection
e	eutectic
f	fusion
i	initial, index
j	index
k	particular phase
l	liquid
liq	liquidus
l_0	reference liquid
m	melting
max.	maximum
min.	minimum
o	outer, external
0	reference
T	thermal
s	solid
tot	total
∞	ambient

Superscripts

J	interfacial
k	CG iteration counter
T	transpose

numerical simulations starting from Flemings [1], and Kurz and Fisher [2], to several other researchers. In recent years, Heinrich and co-workers [3–5], Beckermann et al. [6,7] and Incropera et al. [8,9], have focussed on the

simulation of macrosegregation in binary alloys leading to defects like freckles and channels. Macrosegregation caused by multicomponent thermosolutal convection has been simulated in solidifying steel alloys by Beckermann et al. [10,11] and in Nickel based alloys by Felicelli et al. [12,13]. Three-dimensional simulations of freckle formation have also been carried out in recent years by various researchers [14–16]. Criteria for predicting freckle formation during directional solidification of alloys have been derived by some researchers in recent years based on thermal or solutal Rayleigh numbers [17–19]. The dominant role played by thermosolutal convection in causing macrosegregation was highlighted in these and several other works.

Magnetic fields have been extensively used to damp convection in electrically conducting melts. The convection damping is achieved through the Lorentz force that is produced by induced currents in the moving fluid interacting with the magnetic field lines. Magnetic fields have been extensively used for flow control in crystal growth processes involving semiconductor melts to suppress temperature and concentration fluctuations [20,21]. Ben Hadid et al. [22,23] analyzed the effects of magnetic field on combined thermal buoyancy and thermocapillary driven convection in horizontal Bridgman configurations in two- and three-dimensions to determine important scaling laws for Hartmann flows. In [24], Incropera et al. studied the effects of low magnetic fields on convection and macrosegregation during solidification of a metallic alloy and concluded that the intensity of the magnetic field would have to be sufficiently increased to damp thermosolutal convection effectively. Sampath and Zabaras [25] have studied the effects of magnetic fields on combined thermosolutal and thermocapillary convection during the solidification of alloys. Sampath and Zabaras [26,27] solved an adjoint based inverse problem to design the boundary heat flux during the solidification of metals and alloys in the presence of magnetic fields. Gunzberger et al. [28] solved a design problem to determine the optimal magnetic field required for the suppression of turbulent flow in the melt during crystal growth processes.

In [29,30], an optimization problem was addressed by Zabaras and Ganapathysubramanian where the main objective was to design the time history of the imposed magnetic field to control convection in solidifying melts in the presence of a constant magnetic field gradient. However, while solving such optimization problems, all authors have considered dilute alloys with negligible mushy zones and front tracking methods were used to describe the solid and liquid regions separately.

Box I. Governing equations for solidification of alloys under the influence of magnetic field

$$\nabla \cdot \boldsymbol{v}(\boldsymbol{x},t) = 0, \quad (\boldsymbol{x},t) \in \Omega \times [0, t_{\max}] \tag{1}$$

$$\rho\left(\frac{\partial \boldsymbol{v}(\boldsymbol{x},t)}{\partial t} + \boldsymbol{v}(\boldsymbol{x},t)\nabla \cdot \left(\frac{\boldsymbol{v}(\boldsymbol{x},t)}{\epsilon(\boldsymbol{x},t)}\right)\right) = -\nabla p(\boldsymbol{x},t) + \frac{p(\boldsymbol{x},t)}{\epsilon(\boldsymbol{x},t)}\nabla\epsilon(\boldsymbol{x},t) - \frac{\epsilon\mu}{K(\epsilon)}\boldsymbol{v}(\boldsymbol{x},t) + \nabla \cdot [\mu(\nabla \boldsymbol{v}(\boldsymbol{x},t) + (\nabla \boldsymbol{v}(\boldsymbol{x},t))^{\mathrm{T}})] - \epsilon(\boldsymbol{x},t)\rho_0 g[\beta_{\mathrm{T}}(T(\boldsymbol{x},t) - T_0) + \beta_{\mathrm{C}}(C_{\mathrm{l}}(\boldsymbol{x},t) - C_{\mathrm{l}_0})]\boldsymbol{e_g} + \sigma_{\mathrm{e}}(-\epsilon(\boldsymbol{x},t)\nabla\phi(\boldsymbol{x},t) + (\boldsymbol{v}(\boldsymbol{x},t) \times \mathbf{B})) \times \mathbf{B}, \quad (\boldsymbol{x},t) \in \Omega \times [0, t_{\max}] \tag{2}$$

$$\rho(c_p^* - \mathscr{F})\frac{\partial T(\boldsymbol{x},t)}{\partial t} + \rho c_{p\mathrm{l}}\boldsymbol{v}(\boldsymbol{x},t) \cdot \nabla T(\boldsymbol{x},t) = \nabla \cdot [(\epsilon(\boldsymbol{x},t)k_{\mathrm{l}} + (1 - \epsilon(\boldsymbol{x},t))k_{\mathrm{s}})\nabla T(\boldsymbol{x},t)] - \frac{\rho S^*}{(1 - \kappa_{\mathrm{p}})C_{\mathrm{l}}(\boldsymbol{x},t)}\frac{\partial C(\boldsymbol{x},t)}{\partial t}, \quad (\boldsymbol{x},t) \in \Omega \times [0, t_{\max}] \tag{3}$$

$$\frac{\partial C(\boldsymbol{x},t)}{\partial t} + \boldsymbol{v}(\boldsymbol{x},t) \cdot \nabla C_{\mathrm{l}}(\boldsymbol{x},t) = \nabla \cdot (\epsilon(\boldsymbol{x},t)D_{\mathrm{l}}\nabla C_{\mathrm{l}}(\boldsymbol{x},t)), \quad (\boldsymbol{x},t) \in \Omega \times [0, t_{\max}] \tag{4}$$

$$\nabla \cdot (\epsilon(\boldsymbol{x},t)\nabla\phi(\boldsymbol{x},t) - \boldsymbol{v}(\boldsymbol{x},t) \times \mathbf{B}) = 0, \quad (\boldsymbol{x},t) \in \Omega \times [0, t_{\max}] \tag{5}$$

where

$$\mathscr{F} = \begin{cases} \epsilon(\boldsymbol{x},t)S^*/[(1 - \kappa_{\mathrm{p}})C_{\mathrm{l}}(\boldsymbol{x},t)m_{\mathrm{liq}}], & 0.0 < \epsilon < 1.0 \\ 0, & \epsilon = 1.0 \text{ or } 0.0 \end{cases} \tag{6}$$

$$S^* = (c_{p\mathrm{l}} - c_{ps})(T - T_{\mathrm{e}}) + h_{\mathrm{f}} \quad c_p^* = \epsilon c_{p\mathrm{l}} + (1 - \epsilon)c_{ps} \tag{7}$$

Initial conditions

$$\boldsymbol{v}(\boldsymbol{x},0) = \mathbf{0}, \quad T(\boldsymbol{x},0) = T_i, \quad C(\boldsymbol{x},0) = C_i, \quad \phi(\boldsymbol{x},0) = 0, \quad \boldsymbol{x} \in \Omega \tag{8}$$

The current model utilizes volume-averaged governing transport equations for describing the solidification of an alloy with large mushy zones under the influence of magnetic fields. This model is termed the direct model. The continuum sensitivity problem, is then derived from the direct problem by differentiating governing equations with respect to design variables. To the best of authors knowledge, this is the first time that the continuum sensitivity method (CSM) has been used for alloy solidification problems with mushy zones and an optimization problem attempted taking into account mushy zone permeability that may be isotropic or anisotropic. Previous attempts at optimizing the thermal boundary flux to obtain a desired uniform front growth rate [26,27], or optimizing the value of the magnetic field [28] or the time history of the magnetic field gradient to suppress and damp melt convection [29,30], have all assumed the presence of a sharp interface separating the solid and liquid into two separate and distinct zones.

The organization of the paper is as follows. In Section 2, the underlying mathematical model of the direct problem is first described. In our mathematical model, we include only the magnetic field and not the gradient. Therefore, convection damping occurs as a consequence of Lorentz force caused by the induced current density. In Section 3, continuum sensitivity equations for mushy zone solidification are derived through the continuum sensitivity method (CSM) and the design problem is formulated for obtaining coefficients that determine the time history of the applied magnetic field. Section 4 describes the non-linear conjugate gradient algorithm used for solving the finite-dimensional optimization problem. Numerical techniques and computational methodology used for solving the direct and sensitivity problems are also described briefly in this section. In Section 5, the direct problem is solved and numerical examples that involve convection damping during solidification through the application of constant magnetic fields are discussed. Both two- and three-dimensional examples are discussed here. In Section 6, the continuum sensitivity problem is described using a particular example. Here, sensitivities obtained from CSM are compared with those obtained from finite difference method (FDM) and superior properties of the former are highlighted. The design problem is described after this and examples that involve the design of the time history of the imposed magnetic field for effective convection damping and macrosegregation suppression are considered. This is followed by a section summarizing conclusions and important observations made from the current work.

2. Direct problem

The direct problem describing alloy solidification in the presence of an external magnetic field is first described here. The mathematical model is based on volume-averaged macroscopic equations for transport of heat, mass, flow and solute, and for induced electric potential. Volume-averaged transport equations for mass, momentum, heat and solute were derived in [31] from individual microscopic transport equations and are very similar to continuum solidification models discussed in [3,6,8]. The governing equations are derived by volume averaging the microscopic transport equations of each phase and are listed in Box I. Some of the key assumptions invoked in the alloy solidification model are as follows:

- The liquid is Newtonian and the flow laminar.
- The solid phase is stationary.
- Densities of both phases are equal and constant, except for the Boussinesq approximation in the momentum equations.
- Solute in the liquid is completely mixed and diffusion of solute in the solid is negligible (Scheil rule assumption).
- Pore formation is not modeled in the solidifying alloy and only the solid and liquid phases are present always.
- Individual phase properties like thermal conductivity and specific heat are constant and do not vary with temperature.
- Thermal equilibrium is assumed in the mushy zone, i.e. $T_l = T_s$ in the mushy zone.

The mushy zone is modeled as a porous medium with either an isotropic or anisotropic permeability that is a function of the liquid volume fraction, ϵ. An isotropic permeability is modeled using the Kozeny–Karman relationship given by

$$K(\epsilon) = \frac{K_0 \epsilon^3}{(1-\epsilon)^2} \tag{9}$$

where K_0 is given by $K_0 = d^2/180$, with d being the dendrite arm spacing. When the permeability is assumed to be anisotropic, it is expressed in principal growth directions by

$$K_x(\epsilon) = \begin{cases} 1.09 \times 10^{-3} \epsilon^{3.32} d^2, & \epsilon \leqslant 0.65 \\ 4.04 \times 10^{-6} [\epsilon/(1-\epsilon)]^{6.7336} d^2, & 0.65 < \epsilon \leqslant 0.75 \\ (-6.49 \times 10^{-2} + 5.43 \times 10^{-2} & \\ \quad \times [\epsilon/(1-\epsilon)]^{0.25}) d^2, & 0.75 < \epsilon < 1.0 \end{cases} \tag{10}$$

$$K_y(\epsilon) = K_x(\epsilon) \tag{11}$$

$$K_z(\epsilon) = \begin{cases} 3.75 \times 10^{-4} \epsilon^2 d^2, & \epsilon \leqslant 0.65 \\ 2.05 \times 10^{-7} [\epsilon/(1-\epsilon)]^{10.739} d^2, & 0.65 < \epsilon \leqslant 0.75 \\ 0.074[\log(1-\epsilon)^{-1} - 1.49 + 2(1-\epsilon) & \\ \quad -0.5(1-\epsilon)^2] d^2, & 0.75 < \epsilon < 1.0 \end{cases} \tag{12}$$

Eqs. (10) and (12) express permeability in directions transverse and parallel to the dendrite growth, respectively. These relations are listed in [12–14,16] and have been obtained from experimental data through curve fit and regression analysis. Closure of the numerical model is achieved through thermodynamic expressions that take into account relationships from the phase diagram. For

all our problems, we use the Scheil rule, given below, to describe the evolution of liquid volume fraction

$$\epsilon = \left(\frac{T - T_{\mathrm{m}}}{T_{\mathrm{liq}} - T_{\mathrm{m}}}\right)^{\frac{1}{\kappa_{\mathrm{p}}-1}} \tag{13}$$

where the liquidus temperature, T_{liq}, is expressed as, $T_{\mathrm{liq}} = T_{\mathrm{m}} + m_{\mathrm{liq}}C$, with T_{m} being the melting temperature and m_{liq}, the slope of the liquidus line. κ_{p} denotes the partition coefficient of the alloy. In the mushy zone, the temperature is directly related to liquid solute concentration as $T = T_{\mathrm{m}} + m_{\mathrm{liq}}C_{\mathrm{l}}$. In the model described here, the Lorentz force is the primary force that opposes thermosolutal buoyancy. Key assumptions invoked while coupling the magnetohydrodynamic (MHD) equations with the volume-averaged governing equations are as follows:

- The induced magnetic field is negligible for metallic alloys considered here.
- Phenomenological cross-effects like galvo-magnetic, thermomagnetic and thermoelectric effects are negligible.
- The magnetic field is assumed to be non-relativistic and quasistatic.
- The electric charge density, ρ_{e}, is negligible for the alloys considered here.
- The external magnetic field is spatially invariant.

The mathematical model used here to couple MHD equations with the volume-averaged transport equations is based on the MHD II model described in [32], where induced magnetic fields were neglected and the only magnetic field was the externally applied one. With the quasi-stationary assumption of the magnetic field, the induced electric field, $\mathbf{E}$ is expressed by a potential gradient, $\nabla\phi$, since $\nabla \times \mathbf{E} = 0$. The induced electric potential equation for the liquid phase is derived using the Ohm's law for a moving medium. The derivation of the volume-averaged potential equation is described subsequently.

2.1. Volume-averaged electric potential equation

Motion of an electrically conducting fluid in the presence of a magnetic field gives rise to Lorentz force, which acts to oppose the motion of the fluid. The Lorentz force term, $\mathbf{F}_{\mathrm{Lorentz}}$, is given by

$$\mathbf{F}_{\mathrm{Lorentz}} = \rho_{\mathrm{e}}\mathbf{E} + \mathbf{J} \times \mathbf{B}_{\mathrm{tot}} \tag{14}$$

where ρ_{e} is the electric charge density, $\mathbf{E} = -\nabla\phi$ the induced electric field, ϕ the induced electric potential and $\mathbf{B}_{\mathrm{tot}}$ the magnetic field. The induced electric current density, $\mathbf{J}$, obeys the Ohm's law for a moving medium and is given by

$$\mathbf{J} = \rho_{\mathrm{e}}\boldsymbol{v} + \sigma_{\mathrm{e}}(-\nabla\phi + \boldsymbol{v} \times \mathbf{B}_{\mathrm{tot}}) \tag{15}$$

where σ_{e} is the electrical conductivity and $\boldsymbol{v}$ the velocity vector. The total magnetic field is given by

$$\mathbf{B}_{\mathrm{tot}} = \mathbf{B} + \mathbf{b} \tag{16}$$

where $\mathbf{B}$ is the external applied field and $\mathbf{b}$ the induced field. The magnetic Reynolds number, Re_{m}, is given by $Re_{\mathrm{m}} = \mu_0\sigma_{\mathrm{e}}VL$ and denotes the ratio of the induced to the applied magnetic field. For most liquid metals, $Re_{\mathrm{m}} \ll 1$, and the induced magnetic field $\mathbf{b}$ is negligible compared to the applied magnetic field $\mathbf{B}$. Therefore, assuming $\mathbf{B}_{\mathrm{tot}} \simeq \mathbf{B}$ is reasonable for most problems considered here. Since $\rho_{\mathrm{e}} \ll 1$ in metals, we can neglect terms $\rho_{\mathrm{e}}\mathbf{E}$ and $\rho_{\mathrm{e}}\boldsymbol{v}$ from Eqs. (14) and (15), respectively. Using conservation of electric current, $\mathbf{J}$ obeys

$$\nabla \cdot \mathbf{J} = \mathbf{0} \tag{17}$$

Eqs. (15) and (17) combined together can be re-expressed in terms of ϕ as

$$\nabla^2\phi = \nabla \cdot (\boldsymbol{v} \times \mathbf{B}) \quad \text{in } \boldsymbol{\Omega} \times [\mathbf{0}, \mathbf{t}_{\max}] \tag{18}$$

When more than one phase is present, as in solidification of alloys, the potential equation can be expressed for individual phases as

$$\nabla^2\phi_k = \nabla \cdot (\boldsymbol{v}_k \times \mathbf{B}) \quad \text{in } \boldsymbol{\Omega} \times [\mathbf{0}, \mathbf{t}_{\max}] \tag{19}$$

where the subscript k denotes individual phases (solid or liquid). Eq. (19) is volume-averaged to obtain the governing equation for electric potential.

$$\langle \nabla \cdot (\nabla\phi_k - \boldsymbol{v}_k \times \mathbf{B}) \rangle = 0 \tag{20}$$

where the $\langle\rangle$ denotes the volume-averaging kernel $\frac{1}{\mathrm{d}V}\int_{\mathrm{d}V}(\cdot)\mathrm{d}v$ with $\mathrm{d}V$ consisting of both solid and liquid phases.

Using the volume-averaging identities for divergence, Eq. (20) is simplified as

$$\begin{aligned} &\nabla \cdot \langle (\nabla\phi_k - \boldsymbol{v}_k \times \mathbf{B}) \rangle + \frac{1}{\mathrm{d}V}\int_{\mathrm{d}A_k} (\nabla\phi_k - \boldsymbol{v}_k \times \mathbf{B}) \cdot \mathbf{n}_k \,\mathrm{d}a = 0 \\ &\Rightarrow \nabla \cdot (\langle \nabla\phi_k \rangle - \langle \boldsymbol{v}_k \times \mathbf{B} \rangle) + \frac{1}{\sigma_{\mathrm{e}}\mathrm{d}V}\int_{\mathrm{d}A_k} \mathbf{J}_k \cdot \mathbf{n}_k \,\mathrm{d}a = 0 \end{aligned} \tag{21}$$

where the second term in Eq. (21) is an interfacial flux term of the current density $\mathbf{J}_k$ denoted by I_k^J. The first term in Eq. (21) can be split using volume-averaging identities for gradients and products as

$$\langle \nabla\phi_k \rangle = \epsilon_k \nabla \langle \phi_k \rangle^k + \frac{1}{\mathrm{d}V}\int_{\mathrm{d}V} \hat{\phi}_k \cdot \mathbf{n}_k \,\mathrm{d}a \tag{22}$$

$$\langle \boldsymbol{v}_k \times \mathbf{B} \rangle = \epsilon_k \langle \boldsymbol{v}_k \rangle^{\mathbf{k}} \times \mathbf{B} \tag{23}$$

where ϵ_k is the phase volume fraction. By assuming the potential to be uniform, the microscopic deviation term, $\hat{\phi}_k$, can be neglected. We now make the assumption of balance of interfacial flux terms between different phases, i.e., $\sum_k I_k^J = 0$, for further simplification. By invoking the assumption of a stationary solid phase, the final volume-averaged potential equation is

$$\nabla \cdot (\epsilon_{\mathrm{l}} \nabla \langle \phi_{\mathrm{l}} \rangle^{\mathrm{l}} - \epsilon_{\mathrm{l}} \langle \boldsymbol{v}_{\mathrm{l}} \rangle^{\mathrm{l}} \times \mathbf{B}) = 0 \tag{24}$$

With the microscopic deviation term for velocity being neglected, we have $\langle \boldsymbol{v}_{\mathrm{l}} \rangle^{\mathrm{l}} = \boldsymbol{v}_{\mathrm{l}}$, where $\boldsymbol{v}_{\mathrm{l}}$ is the velocity of

the liquid phase. If densities of the solid and liquid phases are assumed to be equal, the volume and mass fraction of individual phases are equal and the superficial velocity, $\boldsymbol{v}$, is given by $f_l \boldsymbol{v}_l = \epsilon_l \boldsymbol{v}_l$. Also, since the solid is stationary, the induced potential, ϕ_s, in the solid phase is constant and the induced electric field, $\mathbf{E}_s$, responsible for the induced current density, is zero in the solid phase. Therefore, unlike the liquid phase, the solid phase does not experience any body forces. The final governing volume-averaged equation for electric potential is given by

$$\nabla \cdot (\epsilon \nabla \phi - \boldsymbol{v} \times \mathbf{B}) = 0 \tag{25}$$

where ϕ denotes $\langle \phi_l \rangle^1$.

Box I summarizes equations representing the direct problem of alloy solidification under the influence of a magnetic field after incorporating all assumptions discussed in this section.

3. Design problem using tailored magnetic fields

The main objective of the design problem is to create conditions through the application of tailored magnetic fields that result in successful damping of thermosolutal convection and minimization of macrosegregation in the solidifying alloy. This results in a diffusion dominated growth regime that leads to a near homogeneous solute concentration throughout the cast alloy. The definition of the design problem for solidification can therefore be stated as:

Find the time history of the external applied magnetic field $B(t)$ such that the alloy solidification defined by the initial boundary value problem in Box I proceeds with negligible convection resulting in diffusion dominated growth conditions.

With the orientation of the applied magnetic field fixed throughout the solidification process, its magnitude with time is expressed using Bezier–Bernstein polynomials as follows:

$$B(t) = \sum_{i=0}^{N-1} b_i \mathscr{B}_i^{N-1}(\hat{t}) \tag{26}$$

where $\mathscr{B}_i^{N-1}(\hat{t})$ denotes the Bezier–Bernstein polynomial given by

$$\mathscr{B}_i^{N-1}(\hat{t}) = \binom{N-1}{i} \hat{t}^{N-1-i}(1-\hat{t})^i \tag{27}$$

$b_i\,(i = 0, 1, \ldots, N-1)$ denote constant coefficients that form the design space and $\hat{t}$ denotes the non-dimensional time with $\hat{t} = t/t_{\max} \in [0, 1]$. The design space is therefore discretized into a finite-dimensional space of size N. The resultant design problem is therefore reduced to a finite-dimensional optimization problem. Bezier-curves were previously used in [33] to represent complex die shapes during die design problems and capture the effect of small changes in design variables very well. The function space formed by Bezier–Bernstein polynomials was therefore deemed sufficient to capture the time history of the applied magnetic field.

Box II. Continuum sensitivity equations for alloy solidification under the influence of magnetic field

$$\nabla \cdot \overset{\circ}{\boldsymbol{v}} = 0, \quad (\boldsymbol{x}, t) \in \Omega \times [0, t_{\max}] \tag{28}$$

$$\begin{aligned}
&\rho\left[\frac{\partial \overset{\circ}{\boldsymbol{v}}}{\partial t} + \frac{\overset{\circ}{\boldsymbol{v}} \cdot \nabla \boldsymbol{v}}{\epsilon} + \frac{\boldsymbol{v} \cdot \nabla \overset{\circ}{\boldsymbol{v}}}{\epsilon} - \frac{\boldsymbol{v}\boldsymbol{v} \cdot \nabla \overset{\circ}{\epsilon}}{\epsilon^2} + \frac{2\boldsymbol{v}\boldsymbol{v} \cdot \nabla \epsilon \overset{\circ}{\epsilon}}{\epsilon^3}\right] \\
&\quad = -\nabla \overset{\circ}{p} + \frac{\overset{\circ}{p}}{\epsilon}\nabla\epsilon + \frac{p}{\epsilon}\nabla\overset{\circ}{\epsilon} - \frac{p}{\epsilon^2}\overset{\circ}{\epsilon}\nabla\epsilon - \frac{\epsilon\mu}{K(\epsilon)}\overset{\circ}{\boldsymbol{v}} - \frac{\overset{\circ}{\epsilon}\mu}{K(\epsilon)}\boldsymbol{v} + \frac{\epsilon\overset{\circ}{\epsilon}\mu K'(\epsilon)}{K^2(\epsilon)}\boldsymbol{v} + \nabla \cdot [\mu(\nabla \overset{\circ}{\boldsymbol{v}} + (\nabla \overset{\circ}{\boldsymbol{v}})^{\mathrm{T}})] \\
&\qquad - \rho_0 g[\epsilon(\beta_T \overset{\circ}{T} + \beta_C \overset{\circ}{C_l})]\boldsymbol{e_g} - \rho_0 g[\overset{\circ}{\epsilon}(\beta_T(T - T_0) + \beta_C(C_l - C_{l_0}))]\boldsymbol{e_g} \\
&\qquad - \sigma_e[\epsilon(\nabla \overset{\circ}{\phi} \times \mathbf{B}) + \overset{\circ}{\epsilon}(\nabla\phi \times \mathbf{B}) + \epsilon(\nabla\phi \times \Delta\mathbf{B})] \\
&\qquad + \sigma_e[(\overset{\circ}{\boldsymbol{v}} \cdot \mathbf{B})\mathbf{B} - (\mathbf{B} \cdot \mathbf{B})\overset{\circ}{\boldsymbol{v}}] + \sigma_e[(\boldsymbol{v} \cdot \Delta\mathbf{B})\mathbf{B} + (\boldsymbol{v} \cdot \mathbf{B})\Delta\mathbf{B} - 2\boldsymbol{v}(\mathbf{B} \cdot \Delta\mathbf{B})], \quad (\boldsymbol{x}, t) \in \Omega \times [0, t_{\max}]
\end{aligned} \tag{29}$$

$$\begin{aligned}
&\rho\left[c_p^* - \frac{S^*\epsilon}{(1-\kappa_p)(T - T_m)}\right]\frac{\partial \overset{\circ}{T}}{\partial t} + \rho\left[(c_{pl} - c_{ps})\overset{\circ}{\epsilon} - \frac{S^*\overset{\circ}{\epsilon}}{(1-\kappa_p)(T - T_m)}\right]\frac{\partial T}{\partial t} \\
&\quad + \rho\left[\frac{S^*\epsilon\overset{\circ}{T}}{(1-\kappa_p)(T - T_m)^2} - \frac{(c_{pl} - c_{ps})\epsilon\overset{\circ}{T}}{(1-\kappa_p)(T - T_m)}\right]\frac{\partial T}{\partial t} + \rho c_{pl}(\boldsymbol{v} \cdot \nabla \overset{\circ}{T} + \overset{\circ}{\boldsymbol{v}} \cdot \nabla T) \\
&\qquad = \nabla \cdot [(\epsilon k_l + (1-\epsilon)k_s)\nabla \overset{\circ}{T}] + \nabla \cdot [\overset{\circ}{\epsilon}(k_l - k_s)\nabla T] + \frac{\rho S^* m_{liq}\overset{\circ}{T}}{(1-\kappa_p)(T - T_m)^2}\frac{\partial C}{\partial t} - \frac{\rho S^*}{(1-\kappa_p)C_l}\frac{\partial \overset{\circ}{C}}{\partial t} \\
&\qquad\quad - \frac{\rho(c_{pl} - c_{ps})\overset{\circ}{T}}{(1-\kappa_p)C_l}\frac{\partial C}{\partial t}, \quad (\boldsymbol{x}, t) \in \Omega \times [0, t_{\max}]
\end{aligned} \tag{30}$$

$$\frac{\partial \overset{\circ}{C}}{\partial t} + \boldsymbol{v}\cdot\nabla\overset{\circ}{C} + \overset{\circ}{\boldsymbol{v}}\cdot\nabla C_{\mathrm{l}} = \boldsymbol{v}\cdot\nabla(\overset{\circ}{C} - \overset{\circ}{C}_{\mathrm{l}}) + \nabla\cdot(\epsilon D_{\mathrm{l}}\nabla\overset{\circ}{C}_{\mathrm{l}}) + \nabla\cdot(\overset{\circ}{\epsilon} D_{\mathrm{l}}\nabla C_{\mathrm{l}}), \quad (\boldsymbol{x},t)\in\Omega\times[0,t_{\max}] \tag{31}$$

$$\nabla\cdot(\epsilon\nabla\overset{\circ}{\phi}) + \nabla\cdot(\overset{\circ}{\epsilon}\nabla\phi) - \nabla\cdot(\overset{\circ}{\boldsymbol{v}}\times\mathbf{B} + \boldsymbol{v}\times\Delta\mathbf{B}) = 0, \quad (\boldsymbol{x},t)\in\Omega\times[0,t_{\max}] \tag{32}$$

$$\overset{\circ}{C}_{\mathrm{l}} = m_{\mathrm{liq}}\overset{\circ}{T} \tag{33}$$

$$\overset{\circ}{\epsilon} = \frac{1}{1-\kappa_{\mathrm{p}}}\left(\frac{T-T_{\mathrm{m}}}{T_{\mathrm{liq}}-T_{\mathrm{m}}}\right)^{\frac{2-\kappa_{\mathrm{p}}}{\kappa_{\mathrm{p}}-1}} \frac{m_{\mathrm{liq}}\{(T-T_{\mathrm{m}})\overset{\circ}{C} - C\overset{\circ}{T}\}}{(T_{\mathrm{liq}}-T_{\mathrm{m}})^2} \tag{34}$$

where

$$c_p^* = \epsilon c_{p\mathrm{l}} + (1-\epsilon)c_{ps}, \quad S^* = (c_{p\mathrm{l}} - c_{ps})(T-T_{\mathrm{e}}) + h_{\mathrm{f}}, \quad T_{\mathrm{liq}} = T_{\mathrm{m}} + m_{\mathrm{liq}}C, \quad T = T_{\mathrm{m}} + m_{\mathrm{liq}}C_{\mathrm{l}}$$

Initial conditions

$$\overset{\circ}{\boldsymbol{v}}(\boldsymbol{x},0) = \mathbf{0}, \quad \overset{\circ}{T}(\boldsymbol{x},0) = 0, \quad \overset{\circ}{C}(\boldsymbol{x},0) = 0, \quad \overset{\circ}{\phi}(\boldsymbol{x},0) = 0, \quad \boldsymbol{x}\in\Omega \tag{35}$$

3.1. Continuum sensitivity method (CSM)

To achieve significant convection damping and suppression of macrosegregation in a solidifying alloy, the magnetic field must be chosen as to effectively oppose thermosolutal convection that develops during solidification. The cost functional is expressed in terms of the volume-averaged velocity as

$$J = J(B) = J(\{b_i\}) = \frac{1}{2}\int_0^{t_{\max}}\int_\Omega \boldsymbol{v}\cdot\boldsymbol{v}\,\mathrm{d}\Omega\,\mathrm{d}t \tag{36}$$

where B denotes the magnitude of the magnetic field. With the cost functional given by Eq. (36), the objective defined previously can be restated as finding the optimal magnetic field, $\overline{B}(t)$, given by a set of N coefficients, $\bar{b}_0, \bar{b}_1, \ldots, \bar{b}_{N-1}$, such that

$$J(\{\bar{b}_i\}) \leqslant J(\{b_i\}) \quad \forall\ \{b_i\}\in\mathbb{R}^N \tag{37}$$

From the definition of $J(\{b_i\})$ given in Eq. (36), the gradient of J is given by

$$\mathbf{F} = \nabla_b J = \left\{\frac{\partial J}{\partial b_i}\right\} = \int_0^{t_{\max}}\int_\Omega \boldsymbol{v}\cdot\nabla_b\boldsymbol{v}\,\mathrm{d}\Omega\,\mathrm{d}t \tag{38}$$

We define another matrix $\underline{\mathbf{S}}$ ($\underline{\mathbf{S}} = (\mathbf{S_1}, \mathbf{S_2}, \ldots, \mathbf{S_N})^{\mathrm{T}}$) given by

$$\mathbf{S}_i = \frac{\partial\boldsymbol{v}}{\partial b_i} \tag{39}$$

Using Eq. (39), $\mathbf{F}$ is re-expressed as

$$\mathbf{F} = \int_0^{t_{\max}}\int_\Omega \underline{\mathbf{S}}^{\mathrm{T}}\boldsymbol{v}\,\mathrm{d}\Omega\,\mathrm{d}t \tag{40}$$

Box III. Conjugate gradient algorithm for the optimization problem

Step I. Make an initial guess of $\{b\}^0\in\mathbb{R}^N$ defining $B(t)$ and set $k=0$.

Step II. Calculate conjugate search direction $p^k\in\mathbb{R}^N$.

- Solve the coupled direct problem for $\boldsymbol{v}(\boldsymbol{x},t;\{b\}^k)$, $T(\boldsymbol{x},t;\{b\}^k)$, $C(\boldsymbol{x},t;\{b\}^k)$ and $\phi(\boldsymbol{x},t;\{b\}^k)$, and the sensitivity problem for $\overset{\circ}{\boldsymbol{v}}(\boldsymbol{x},t;\{b\}^k)$, $\overset{\circ}{T}(\boldsymbol{x},t;\{b\}^k)$, $\overset{\circ}{C}(\boldsymbol{x},t;\{b\}^k)$ and $\overset{\circ}{\phi}(\boldsymbol{x},t;\{b\}^k)$.
- Calculate $J(\{b\}^k)$ and $\mathbf{F}(\{b\}^k)$ functional defined by Eqs. (36) and (38); if $\mathscr{J} = J(\{b\}^k)/J(\{b\}^0) \leqslant$ tolerance, set $\{b\} = \{b\}^k$ and stop.
- Set $\gamma^k = 0$, if $k=0$; Otherwise $\gamma^k = \frac{\mathbf{F}(\{b\}^k)^{\mathrm{T}}(\mathbf{F}(\{b\}^k)-\mathbf{F}(\{b\}^{k-1}))}{\mathbf{F}(\{b\}^{k-1})^{\mathrm{T}}\mathbf{F}(\{b\}^{k-1})}$.
- Define p^k, if $k=0$, $p^0 = -\mathbf{F}(\{b\}^0)$; Otherwise $p^k = -\mathbf{F}(\{b\}^k) + \gamma_k p^{k-1}$.

Step III. Calculate the optimal step size α^k given by $\alpha^k = -\frac{p^{k\mathrm{T}}\mathbf{F}(\{b\}^k)}{p^{k\mathrm{T}}\mathbf{M}p^k}$. The sensitivity matrix, $\mathbf{M}$, is given by $M_{ij} = \int_0^{t_{\max}}\int_\Omega \frac{\partial\boldsymbol{v}}{\partial b_i}\cdot\frac{\partial\boldsymbol{v}}{\partial b_j}\,\mathrm{d}\Omega\,\mathrm{d}t$.

Step IV. Update $b_i^{k+1} = b_i^k + \alpha^k p^k,\ i = 0,\ldots,N-1$.

Step V. Set $k = k+1$ and return to Step II.

The continuum sensitivity method (CSM) is used for obtaining the continuum sensitivity (CS) equations that provide the gradient information required in the optimization algorithm. If ΔB represents the perturbation in the magnitude of the imposed magnetic field, $B(t)$, the perturbed direct fields are given by $T(\boldsymbol{x},t;B+\Delta B)$, $C(\boldsymbol{x},t;B+\Delta B)$, $\boldsymbol{v}(\boldsymbol{x},t;B+\Delta B)$ and $\phi(\boldsymbol{x},t;B+\Delta B)$. The corresponding sensitivity fields are then expressed as follows:

$$T(\boldsymbol{x},t;B+\Delta B)=T(\boldsymbol{x},t;B)+\overset{\circ}{T}(\boldsymbol{x},t;B,\Delta B)+\mathrm{O}(\|\Delta B\|^2) \tag{41}$$

$$\boldsymbol{v}(\boldsymbol{x},t;B+\Delta B)=\boldsymbol{v}(\boldsymbol{x},t;B)+\overset{\circ}{\boldsymbol{v}}(\boldsymbol{x},t;B,\Delta B)+\mathrm{O}(\|\Delta B\|^2) \tag{42}$$

$$C(\boldsymbol{x},t;B+\Delta B)=C(\boldsymbol{x},t;B)+\overset{\circ}{C}(\boldsymbol{x},t;B,\Delta B)+\mathrm{O}(\|\Delta B\|^2) \tag{43}$$

$$\phi(\boldsymbol{x},t;B+\Delta B)=\phi(\boldsymbol{x},t;B)+\overset{\circ}{\phi}(\boldsymbol{x},t;B,\Delta B)+\mathrm{O}(\|\Delta B\|^2) \tag{44}$$

where the sensitivity temperature, sensitivity concentration, sensitivity velocity and sensitivity potential are denoted by $\overset{\circ}{T}$, $\overset{\circ}{C}$, $\overset{\circ}{\boldsymbol{v}}$ and $\overset{\circ}{\phi}$, respectively.Terms second order in ΔB are neglected.By taking directional derivatives of the governing equations described in Box I in the direction of ΔB and evaluating them at $T(\boldsymbol{x},t;B)$, $C(\boldsymbol{x},t;B)$, $\phi(\boldsymbol{x},t;B)$, $p(\boldsymbol{x},t;B)$ and $\boldsymbol{v}(\boldsymbol{x},t;B)$ corresponding to the imposed magnetic field $B(t)$, we obtain governing equations for the linear sensitivity solidification problem.These equations are summarized in Box II with the main unknown variables here being $\overset{\circ}{T}$, $\overset{\circ}{C}$, $\overset{\circ}{p}$, $\overset{\circ}{\boldsymbol{v}}$, and $\overset{\circ}{\phi}$.In addition to Eqs.(28)–(32), two more auxiliary relationships given by Eqs.(33) and (34) express the sensitivity liquid solute concentration, $\overset{\circ}{C}_{\mathrm{l}}$, and the sensitivity liquid volume fraction, $\overset{\circ}{\epsilon}$, respectively in terms of other known sensitivity variables.Both these equations are derived using closure and phase diagram relationships described in Section 2.Gradient based methods are used to solve the optimization problem.Gradient fields are evaluated from sensitivity fields obtained after solving the continuum sensitivity problem.Consider any field $\mathbf{Y}$ whose sensitivity, $\overset{\circ}{\mathbf{Y}}$, has been obtained after solving the sensitivity problem for a particular choice of infinitesimally small and a priori specified perturbations, $\Delta b_i, i=1,2,\ldots,N$. $\mathbf{Y}$ can be expressed as

$$\overset{\circ}{\mathbf{Y}}(\boldsymbol{x},t;b_1,\ldots,b_N,\Delta b_1,\ldots,\Delta b_N)=\sum_{i=1}^{N}\frac{\partial\mathbf{Y}}{\partial b_i}\Delta b_i \tag{45}$$

Therefore, we have

$$\frac{\partial\mathbf{Y}}{\partial b_i}=\frac{\overset{\circ}{\mathbf{Y}}(\boldsymbol{x},t;b_1,b_2,\ldots,b_N,0,0,\ldots,\Delta b_i,\ldots,0)}{\Delta b_i} \tag{46}$$

The computation of the gradient of any field requires the solution of N CSM problems. Therefore, the solution of the design problem requires the sequential solution at each time step of the direct problem and N linear sensitivity problems corresponding to each design variable. The procedure to obtain gradient fields from sensitivity fields is the same as that described in Section 4.2 of [33], where the continuum sensitivity method was used for the design of deformation processes.

4. Computational techniques

A non-linear conjugate gradient algorithm based on the Polak-Ribiere method used to solve the optimization problem is summarized in Box III. The algorithm shown here is nearly identical to that used in [29,30] for an adjoint based design problem except in the definition of the sensitivity matrix and inner products, which are similar to those described in [33] for a CSM-based finite-dimensional optimization problem. For the direct problem, stabilized finite element methodologies are used to discretize the governing transport equations of fluid flow, heat and solute. A modified form of SUPG–PSPG based stabilized finite element technique for discretizing the fluid flow problem in alloy solidification systems, previously developed in [34,35], is used in this work. Thermal and solute species governing equations are discretized by SUPG based finite element methods. Supplementary thermodynamic and two-phase relationships are used to update volume fractions and solute concentrations in individual phases. The multistep predictor–corrector scheme is used for thermal and solute problems, while the Newton–Raphson scheme along with a global line search method is used for the fluid flow problem.

The solution of the direct problem is similar to the numerical scheme described in [34]. Velocity, $\boldsymbol{v}$, temperature, T, solute concentration, C and pressure, p fields are obtained after solving the direct problem and liquid solute concentration, C_{l}, and liquid volume fraction fields, ϵ are obtained from thermodynamic and phase diagram relationships. At each time step, in an inner iteration loop the thermal and solutal sub-problems are solved repeatedly to converge liquid solute concentration and liquid volume fraction fields. The flow and the induced electric potential sub-problems are solved only once in a particular time step with the latter solved after the former. Once the direct problem is fully solved, the solution of individual sensitivity problems proceeds. In each sensitivity problem, the sensitivity heat, sensitivity solute, sensitivity flow and sensitivity potential sub-problems are solved. Solution of the linear sensitivity sub-problems is much simpler compared to their direct counterparts. At each time step, in an inner iteration loop, the sensitivity heat and sensitivity solute sub-problems are solved repeatedly to converge the sensitivity liquid solute concentration, $\overset{\circ}{C}_{\mathrm{l}}$ and sensitivity liquid volume fraction, $\overset{\circ}{\epsilon}$, fields. After that, the sensitivity flow and the sensitivity potential sub-problems are solved.

5. Numerical examples – direct problem

In this section, examples describing the direct problem involving constant magnetic fields are first discussed. The main aim here is to highlight the role of magnetic fields in damping convection and suppressing macrosegregation during alloy solidification. Both two- (2D) and three-dimensional (3D) examples are considered to show the effectiveness of magnetic fields in damping convection during alloy solidification. Due to our emphasis on macrosegregation, the overall concentration of the solute is shown for all examples instead of individual phase concentrations.

5.1. Validation problem for the MHD alloy solidification model

To validate the MHD based alloy solidification model, horizontal solidification of a lead–tin alloy in a copper mold under a constant magnetic field intensity of 0.5 T is first considered. The composition of the alloy is 19% by weight tin (solute) and rest lead. Initially, both the mold and the melt are at 578 K. Heat is removed from the left wall. The convective heat transfer coefficient and the ambient temperature are selected as 50 W m^{-2} K^{-1} and 286 K, respectively, here. This problem was previously addressed by Incropera et al. [24] for two different magnetic field intensities, 0.5 T and 0.1 T, to demonstrate the effect of magnetic fields on thermosolutal convection and macrosegregation. Fig. 1 shows the domain and boundary conditions for this problem. Neumann boundary conditions are applied for the concentration of tin and induced electric potential fields on all boundaries. A magnetic field of 0.5 T is applied in the positive z direction opposite to that of gravity. The shaded region denotes the mold and the solidification occurs from the left wall. Some of the important physical parameters characterizing this problem are given in Table 1. Dimensions of the cavity and thermal properties of the mold are given in Tables 2 and 3, respectively. Perfect contact between the metal and the mold is assumed throughout the solidification process. A 66×68 mesh consisting of quadrilateral bilinear elements was initially used for this problem. Fig. 2 shows the temperature, concentration of tin, volume fraction and velocity fields at time $t = 210$ s which is similar to those observed in [24]. Comparison of maximum velocity magnitudes are given in Table 4. The problem was repeated after increasing the mesh density to 71×78. Fig. 3 shows the macrosegregation patterns at $t = 600$ s after complete solidification for both grids indicating a convergence in our numerical results. It is observed that, in spite of the presence of magnetic field, channel formation is not suppressed and significant macrosegregation occurs due to thermosolutal convection that is not entirely damped. Therefore, to eliminate macrosegregation significantly, increasing the magnetic field intensity to an order of 5 T or above, as recommended in [24], is necessary.

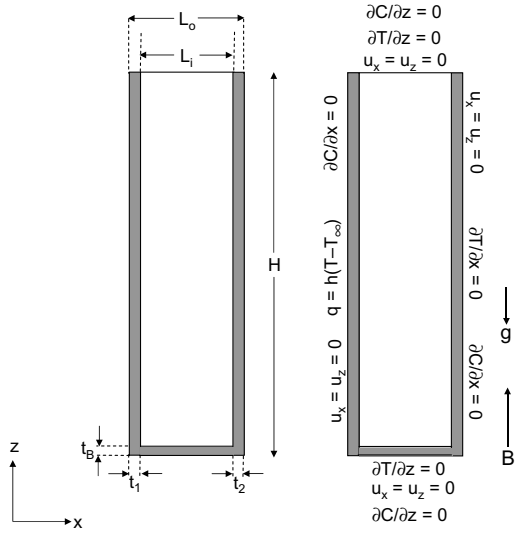

Fig. 1. Domain and boundary conditions for the validation problem. $\partial\phi/\partial n = 0$ on all boundaries (where $n = x$ and z).

Table 1
Important physical parameters for lead–tin alloy

Symbol	Value	Units
k_s	1.855×10^{-2}	kW m^{-1} K^{-1}
k_l	1.855×10^{-2}	kW m^{-1} K^{-1}
c_s	0.167	kJ kg^{-1} K^{-1}
c_l	0.167	kJ kg^{-1} K^{-1}
h_f	37.6	kJ kg^{-1}
κ_p	0.31	
β_T	1.2×10^{-4}	K^{-1}
β_C	0.515	$(kg/kg)^{-1}$
ρ_s	1.01×10^{4}	kg m^{-3}
ρ_l	1.01×10^{4}	kg m^{-3}
μ	2.495×10^{-3}	kg m^{-1} s^{-1}
T_e	456.0	K
T_m	600.0	K
g	9.81	m s^{-2}
m_{liq}	−2.33	K (wt%$^{-1}$)
D_l	3×10^{-9}	m^2 s^{-1}
σ_e	1.5×10^{6}	Ohm^{-1} m^{-1}

Table 2
Dimensions (in mm) of the cavity of Example 5.1

H	L_0	L_i	t_1	t_2	t_B
157.95	52.31	46.87	2.31	3.12	7.95

Table 3
Properties of the mold material in Example 5.1

ρ (kg/m^3)	$c_{p_{mold}}$ (kJ/kg K)	k_{mold} (kW/m K)
7900	0.535	0.018

5.2. 2D horizontal solidification of a metal alloy

We now consider convection damping during horizontal solidification of a lead–10% by weight tin alloy where the

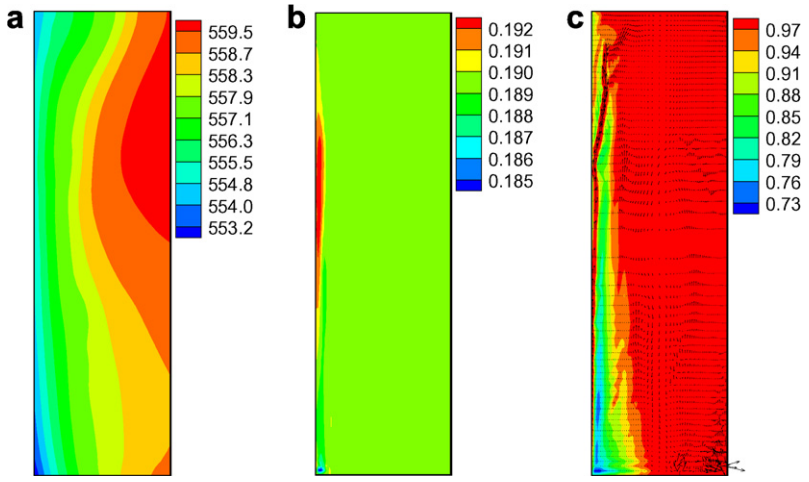

Fig. 2. (a) Isotherms, (b) concentration of tin and (c) liquid volume fraction and velocity fields at $t = 210$ s for Example 5.1, $v_{max} = 3.89$ mm/s.

Table 4
Comparison between maximum velocity magnitudes at two different times

Time (s)	$v_{\|max\|}$ (mm/s) calculated here	$v_{\|max\|}$ (mm/s) from [24]
170	17.5	15.6
210	3.89	3.58

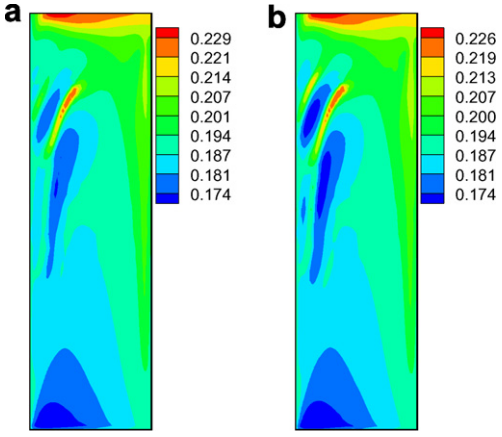

Fig. 3. Concentration of tin at $t = 600$ s for (a) 66×68 mesh and (b) 71×78 mesh.

solute is tin. The magnetic field intensity is increased to 5 T here and it is applied in the positive z direction, opposite to the direction in which gravity acts. Fig. 4 shows the domain and boundary conditions used for simulating this problem. The mushy zone permeability is assumed to be isotropic and given by the Kozeny–Karman relationship given in Eq. (9). The initial temperature (T_i) of the melt is 580 K. Heat is removed from the left wall and all other walls are insulated. The convective heat transfer coefficient and the ambient temperature are selected as 1000 W m^{-2} K^{-1} and 298 K, respectively, here. No-slip and no penetration boundary conditions are assumed for the fluid flow problem. Neumann boundary conditions are applied for the tin concentration and induced electric potential fields on

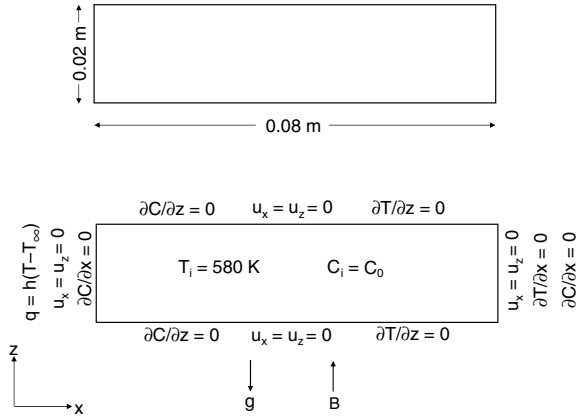

Fig. 4. Domain and boundary conditions for the 2D Pb–Sn alloy solidification problem. $C_0 = 10\%$ by wt. Sn and $T_0 = T_{liq}$. $\partial\phi/\partial n = 0$ on all boundaries.

all boundaries. This example is characterized by strong thermosolutal buoyancy that drives convection and leads to severe macrosegregation throughout the cavity. A mesh consisting of 4590 quadrilateral elements was used for this problem. Fig. 5(a)–(c) and Fig. 6(a)–(c) show the temperature, concentration of tin (solute), liquid volume fraction and velocity fields for magnetic field intensities of 0 T and 5 T, respectively, at $t = 120$ s. The presence of the magnetic field helps in damping out thermosolutal convection significantly as evident from maximum velocity magnitudes listed in Table 5 for both cases at few different times. Moreover, macrosegregation that is particularly severe as observed from Fig. 5(b) is significantly suppressed. This example is used in Section 6 for an optimization problem involving the design of the time history of the applied magnetic field.

5.3. 2D vertical directional solidification of a metal alloy

In this example, we consider a lead–tin alloy directionally solidifying in a vertical cavity as shown in Fig. 7. The

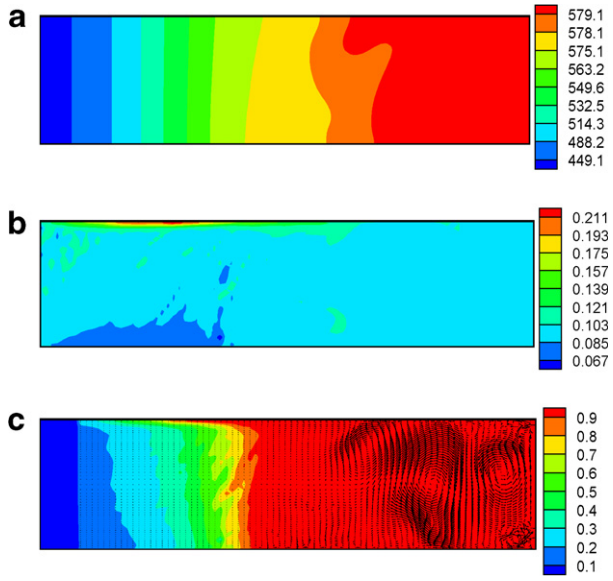

Fig. 5. (a) Temperature, (b) concentration of tin and (c) liquid volume fraction and velocity at $t = 120$ s (no magnetic field) in Example 5.2.

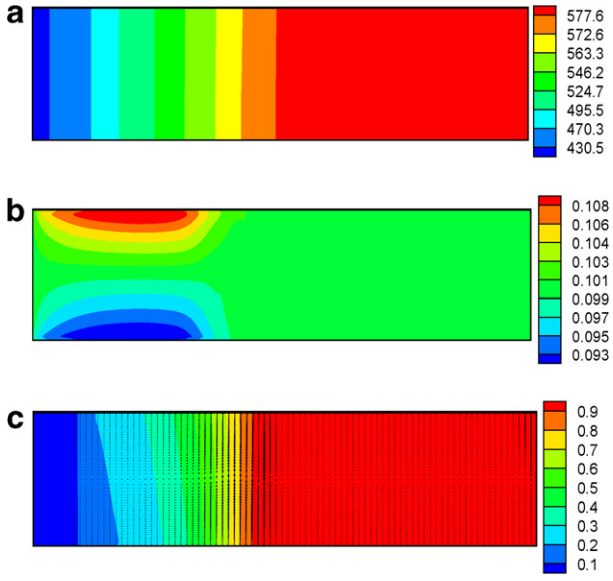

Fig. 6. (a) Temperature, (b) concentration of tin and (c) liquid volume fraction and velocity at $t = 120$ s (magnitude of magnetic field = 5 T) in Example 5.2.

Table 5
Comparison of maximum velocity magnitudes at two different times for magnetic fields of 0 T and 5 T in Example 5.2

Time (s)	$v_{\|max\|}$ (mm/s) (no magnetic field)	$v_{\|max\|}$ (mm/s) (magnetic field = 5 T)
40	74.3	0.331
120	96.9	0.382
160	189.3	0.186

mushy zone permeability is assumed to be anisotropic with the permeability given by Eqs. (10) and (12). A magnetic field intensity of 3.5 T is applied in the x direction. Fig. 7 shows the domain and boundary conditions for this particular problem. A uniform vertical temperature gradient, G, is applied throughout the cavity and the cooling rate, r, at the bottom of the cavity is constant. Fig. 8(a)–(d) shows the concentration of tin (solute), liquid volume fraction and velocity fields at time $t = 800$ s for both magnetic field intensities of 0 and 3.5 T. During directional solidification, channel formation occurs due to thermosolutal convection as observed in Fig. 8(a) and (b). This leads to the formation of freckles in the final cast alloy. The solute concentration in these regions varies greatly compared to the bulk and results in non-uniform properties in the final cast alloy. Channel formation is suppressed through the application of magnetic fields as observed from Fig. 8(c) and (d). Thermosolutal convection is suppressed and the solute distribution is more uniform here.

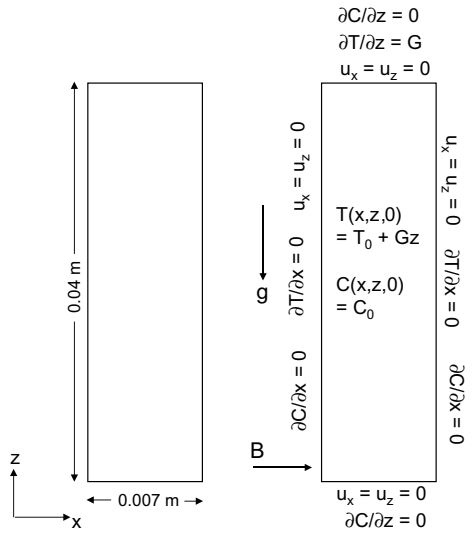

Fig. 7. Domain and boundary conditions for the directional solidification problem. Uniform vertical thermal gradient, $G = 7700$ K/m, bottom cooling rate ($\partial T/\partial t$), $r = 0.2$ K/s, $C_0 = 10\%$ by wt. Sn and $T_0 = T_{liq}$. $\partial\phi/\partial n = 0$ on all boundaries.

5.4. 3D vertical directional solidification of a metal alloy

We now consider convection damping for a three-dimensional directional solidification of a metallic alloy. The problem domain along with the boundary conditions is shown in Fig. 9. No-slip, no penetration conditions for velocity and Neumann conditions for the induced electric potential and solute (tin) concentration are assumed on all faces. All side faces are assumed to be thermally insulated. The mushy zone permeability is assumed to be anisotropic with the permeability given by Eqs. (10)–(12). Like the previous example, the cavity is characterized by a uniform vertical temperature gradient, G, a constant cooling rate, r, at the bottom face. Figs. 10 and 11 show the concentration and liquid volume fraction fields at time

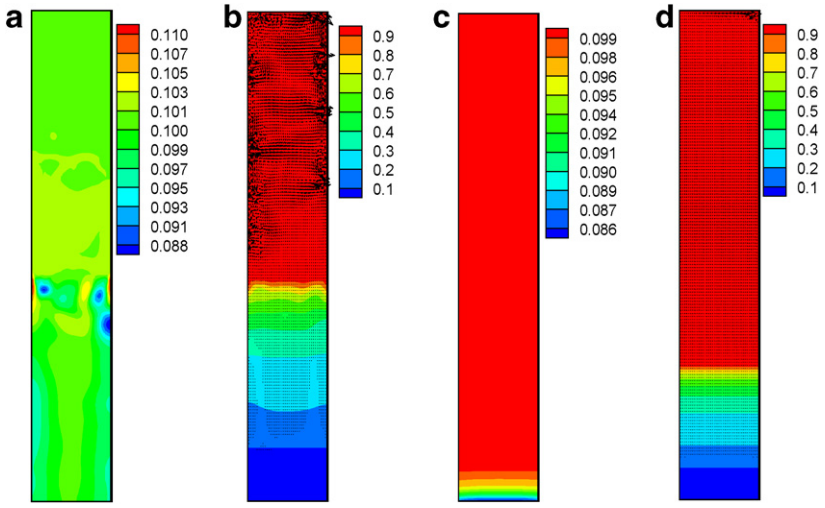

Fig. 8. No magnetic field – (a) concentration of tin, (b) liquid volume fraction and velocity. Magnetic field of 3.5 T – (c) concentration of tin, (d) liquid volume fraction and velocity.

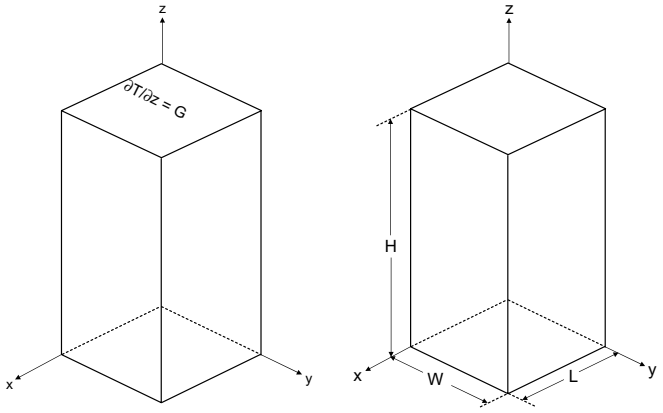

Fig. 9. Problem domain for Example 5.4. Uniform vertical thermal gradient, $G = 1000$ K/m, bottom cooling rate ($\partial T/\partial t$), $r = 0.0167$ K/s, $C_0 = 10\%$ by wt. Sn and $T_0 = T_{liq}$. All side faces are thermally insulated. $\partial C/\partial n = 0$ and $\partial \phi/\partial n = 0$ on all boundaries (where $n = x$, y and z). $v_x = v_y = v_z = 0$ on all faces.

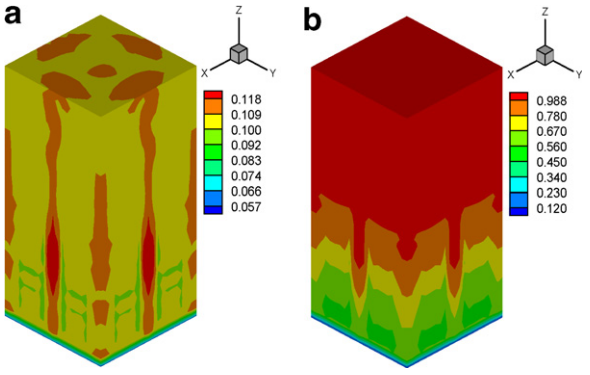

Fig. 10. (a) Concentration of tin and (b) liquid volume fraction at $t = 800$ s (no magnetic field) for Example 5.4.

$t = 800$ s for magnetic fields of 0 and 5 T, respectively. In the absence of magnetic field, channel formation occurs

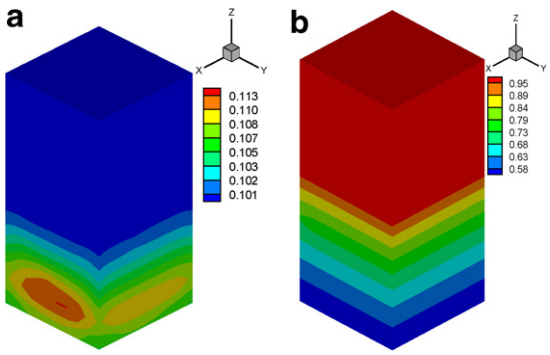

Fig. 11. (a) Concentration of tin and (b) liquid volume fraction at $t = 800$ s (magnetic field = 5 T) for Example 5.4.

in the bulk leading to the formation of freckle defects where solute concentration differs greatly compared to the bulk as observed from Fig. 10(a) and (b). Freckles develop faster and become more prominent after $t = 500$ s. The application of a magnetic field suppresses channel formation by damping out thermosolutal convection throughout the solidification process. This is evident from Fig. 11(a) and (b). Macrosegregation is eliminated and solute concentration is nearly uniform throughout the cavity. This example is also used in Section 6 for demonstrating the design of the time history of applied magnetic fields for alloy solidification in three dimensions.

6. Numerical examples – optimization problem

In this section, the comparison of sensitivity fields from the continuum sensitivity method (CSM) and finite difference method (FDM) is provided. Next, design problems are considered where the time history of the imposed magnetic field is determined by solving a finite-dimensional optimization problem.

6.1. Comparison of sensitivities from CSM and FDM methods

The CSM equations are derived by differentiating the governing equations for the direct problem with respect to design variables and are shown in Box II. CSM validation is done using the example discussed in Section 5.2 by comparing sensitivity fields for two different mesh sizes of 4000 and 4590 elements. Sensitivity values remained unchanged for both of these mesh sizes. Sensitivities obtained from CSM are then compared with those obtained from the finite difference method. The reference magnetic field, B_0 is chosen as 2 T, while the perturbation, ΔB, is chosen as either 0.05 T or -0.05 T. Sensitivities in the FD method are obtained by taking the difference between various field variables from two direct problems run with magnetic fields, B_0 and $B_0 + \Delta B$, respectively. Figs. 12 and 13 summarize different sensitivity fields for the CS and FD methods, respectively, with ΔB being 0.05 T. From these figures, it is evident that both the FD and CS methods capture sensitivity fields well. However, sensitivities from FDM appear to be polluted with numerical noise when compared to those obtained from CSM. The latter is therefore used for obtaining sensitivities in the optimization problems considered subsequently.

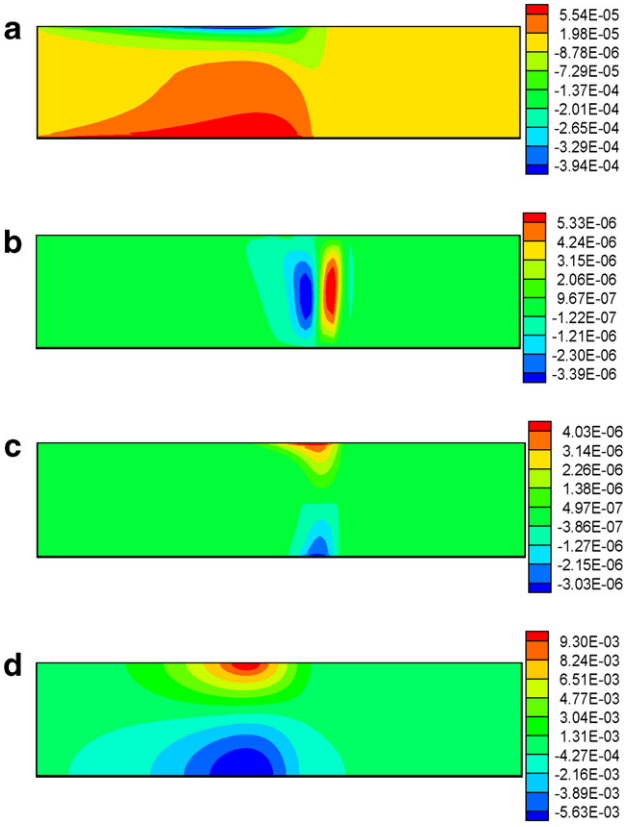

Fig. 12. Sensitivity fields of (a) concentration of tin, (b) horizontal velocity, (c) vertical velocity and (d) temperature at $t = 120$ s (continuum sensitivity method) with $B_0 = 2$ T and $\Delta B = 0.05$ T.

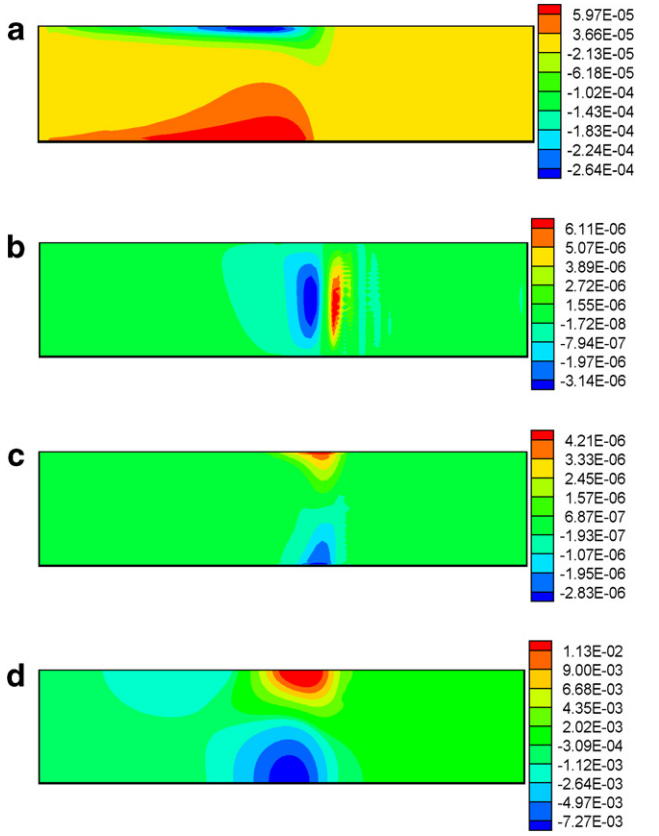

Fig. 13. Sensitivity fields of (a) concentration of tin, (b) horizontal velocity, (c) vertical velocity and (d) temperature at $t = 120$ s (finite difference method) with $B_0 = 2$ T and $\Delta B = 0.05$ T.

6.2. Optimization problem for a 2D horizontal solidification problem

The first optimization considered is the design of time history of the external magnetic field for convection damping during the two dimensional horizontal solidification of a lead–tin alloy that was previously addressed in Section 5.2. This problem is characterized by strong thermosolutal buoyancy forces and severe convection driven macrosegregation in the solidifying alloy. The optimization problem was solved using four and five design variables that use third and fourth degree Bezier–Bernstein curves, respectively. The initial guess is chosen as a magnetic field of 0.4 T constant in time with $b_i = 0.4$. The relative tolerance (J_k/J_0) during the optimization process for terminating the non-linear CG iterations was chosen as 10^{-3}. The time interval under consideration is given by $t \in [0, 120]$. Figs. 14 and 15 show the cost functional variation for both these cases. Figs. 16 and 17 show the variation of the optimal magnetic field under the time interval considered here. The optimal magnetic field is captured well by both design space discretizations. It is higher in the initial stages to counter the strong thermosolutal buoyancy force, prevalent initially. Under the combined influence of thermosolutal buoyancy and Lorentz forces the convection weakens with time and the magnetic field decreases with time

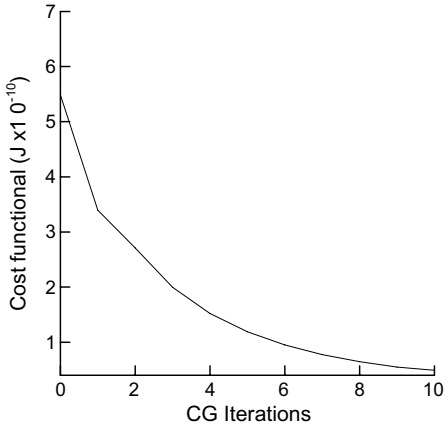

Fig. 14. Cost functional versus CGM iteration for Example 6.2 (four design variables).

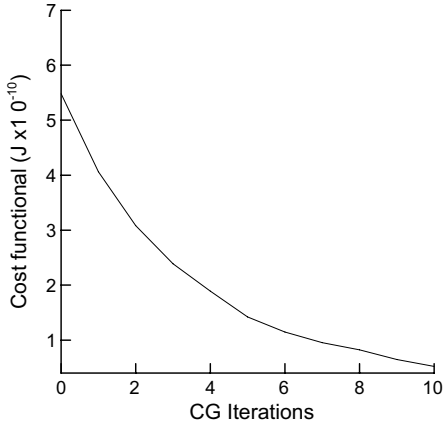

Fig. 15. Cost functional versus CGM iteration for Example 6.2 (five design variables).

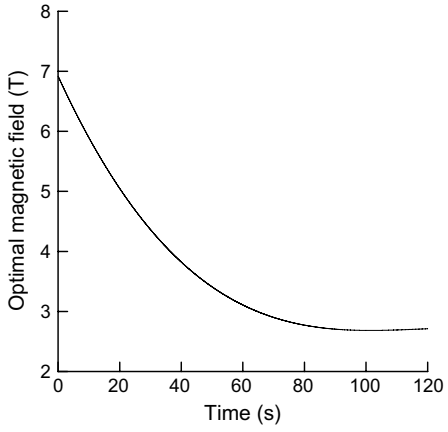

Fig. 16. Plot of the optimal magnetic field for Example 6.2 (four design variables).

accordingly. The magnetic field approaches a final asymptotic value, lower than its starting magnitude, towards the end of the time interval that is required to suppress weaker thermosolutal convection in the later stages. The Darcy

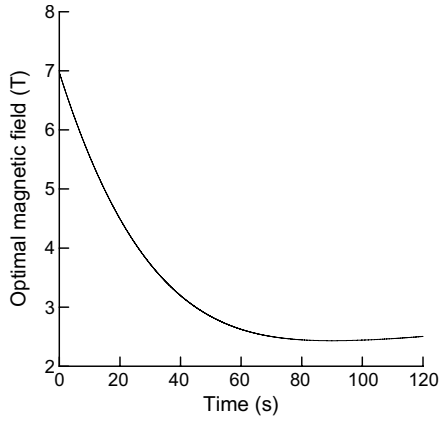

Fig. 17. Plot of the optimal magnetic field for Example 6.2 (five design variables).

drag force that appears in the mushy zone during solidification contributes to velocity damping in that zone. All these factors eliminate the need to maintain a constant high field throughout the solidification process. Table 6 shows the difference between the maximum and minimum solute concentrations, ΔC, at two different times. Fig. 18(a)–(c) shows

Table 6
Comparison of ΔC at two different times for Example 6.2 with no, constant and optimal magnetic fields ($\Delta C = C_{max} - C_{min}$ and number of design variables = 5)

	ΔC (% Sn) ($t = 60$ s)	ΔC (% Sn) ($t = 120$ s)
No magnetic field	13.35	17.57
Magnetic field of 5 T	1.06	1.94
Optimal magnetic field	0.92	1.52

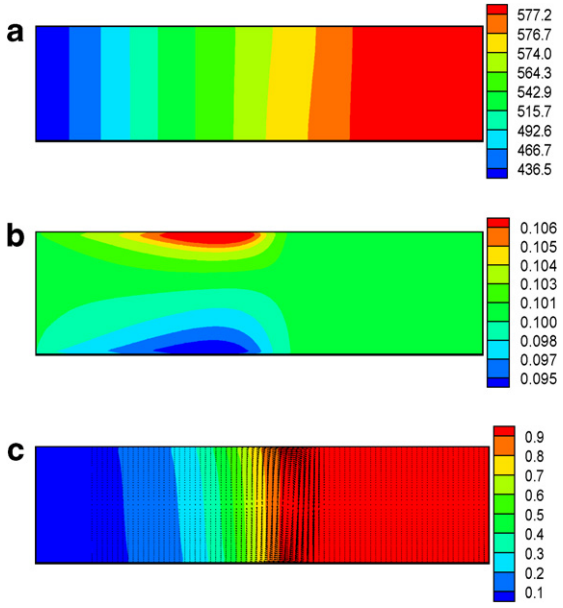

Fig. 18. (a) Temperature, (b) concentration of tin and (c) liquid volume fraction and velocity at $t = 120$ s for Example 6.2 (for the optimal magnetic field obtained with five design variables).

different field variables under the influence of the optimal magnetic field at $t = 120$ s. From these figures, it is clear that the application of the optimal magnetic field helps in damping out thermosolutal convection significantly leading to a diffusion dominated growth regime. From Fig. 18(b) and Table 6 it is evident that macrosegregation is suppressed to a large extent and the solute concentration profile in the solidifying alloy is more uniform in the presence of the optimal field than that observed in Fig. 5(b) in the absence of any field. In fact, from Table 6, a marginally higher reduction in the degree of segregation (ΔC) is observed for an optimal magnetic field than for a constant magnetic field.

6.3. Optimization problem for a 3D directional solidification problem

The second optimization problem considered involves designing the time history of the applied magnetic field during the three-dimensional directional solidification of a lead–tin alloy addressed previously in Section 5.4. The time interval considered here is given by $t \in [0, 800]$ and the number of design variables is 4 here. The initial guess is chosen as a magnetic field of 1.5 T constant in time with $b_i = 1.5$. The relative tolerance during the optimization process for terminating the non-linear CG iterations was chosen as 10^{-3}. Fig. 19 shows the cost functional and Fig. 20 shows the variation of the optimal magnetic field under the time interval considered. The time variation is very similar to that observed in the previous example. The magnitude of the applied field, which is higher in the initial stages to suppress stronger thermosolutal buoyancy forces, decreases with time. Towards the end, there is a marginal increase in magnetic field, but it is lower than the starting magnitude. This is required to counter the residual solutal convection that is responsible for freckle formation and growth at later times. Fig. 21(a) and (b) shows the solute concentration and liquid volume fraction fields for the optimal magnetic field. The optimal magnetic field is successful in suppressing channel formation and

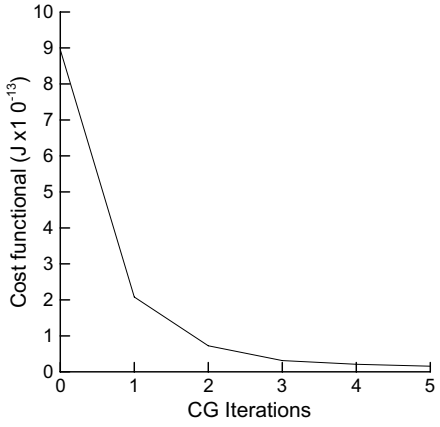

Fig. 19. Cost functional versus CG iteration for Example 6.3.

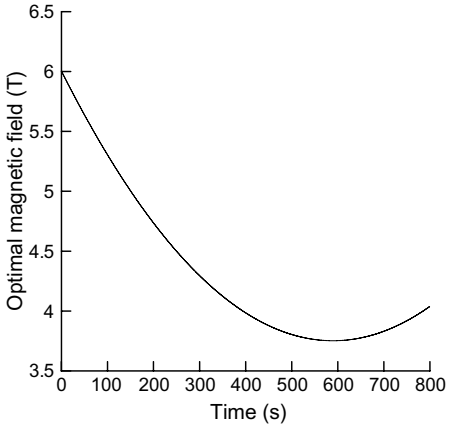

Fig. 20. Plot of the optimal magnetic field obtained with four design variables for Example 6.3.

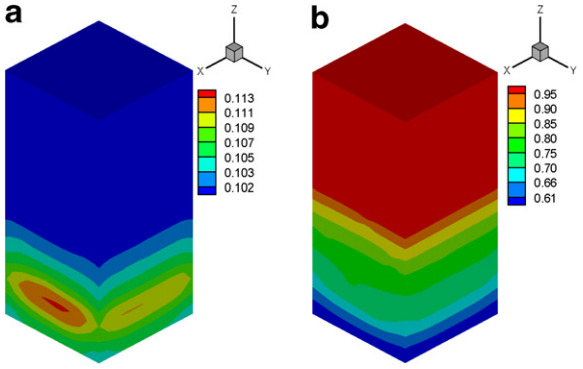

Fig. 21. (a) Concentration of tin and (b) liquid volume fraction at $t = 800$ s (optimal time varying magnetic field) for Example 6.3.

Table 7
Comparison of ΔC at two different times for Example 6.3 with zero, constant and optimal magnetic fields ($\Delta C = C_{max} - C_{min}$ and number of design variables = 4)

	ΔC (% Sn) ($t = 400$ s)	ΔC (% Sn) ($t = 800$ s)
No magnetic field	5.97	7.40
Magnetic field of 5 T	0.57	1.78
Optimal magnetic field	0.40	1.65

inhibiting macrosegregation that were previously observed in Fig. 10(a) and (b) in the absence of any magnetic field and also in Table 7, where ΔC values at two different times are tabulated. The need to maintain a constant high magnetic field throughout the solidification process is also eliminated. Like in the previous example, the margin of reduction in the degree of segregation (ΔC) is slightly better with the optimal magnetic field than with a constant magnetic field of 5 T.

7. Conclusions

A numerical study of the effect of magnetic fields on solidification of metallic alloys with significant mushy

zones was presented. The direct problem was based on a single domain volume-averaged model for alloy solidification under the influence of magnetic fields. Based on this, a continuum sensitivity based finite-dimensional optimization problem was formulated for designing the time history of the externally imposed magnetic fields. The main objective here was to use an optimal magnetic field to suppress thermosolutal convection and inhibit macrosegregation during alloy solidification. The orientation of the applied magnetic field was fixed and only the magnitude was chosen to vary with time. For metallic alloys considered here, the Lorentz force arising due to the application of magnetic fields on moving melts is the primary damping force. Once solidification starts, Darcy drag forces appear in the mushy zone and they contribute to velocity damping in that zone. The cost functional minimization was carried out using a non-linear conjugate gradient method that utilized finite element solutions of the continuum direct and sensitivity problems. The magnetic field was tailored so as to capture variations in thermosolutal convection during solidification of the alloy. The magnitude of the optimal magnetic field was higher during the initial stages of solidification and decreased with time before approaching an asymptotic value for the 2D example or increasing slightly towards the end of the time interval considered for the 3D example. During 3D directional solidification, this increase is necessary to counter the solutal convection that is responsible for freckle formation and growth at later times. The use of an optimal magnetic field alleviates the need to use a constant high magnetic field throughout the solidification process, which in turn translates into power and energy savings. Optimization examples in both two and three dimensions were considered to highlight the efficacy and dimension independent nature of the design simulator.

Acknowledgements

The work presented here was funded by the University–Industry Partnerships for Aluminum Industry of the Future Program of the Office of Industrial Technologies of the US Department of Energy (DE-FC07-02ID14396) with additional matching support from Alcoa. This research was conducted using the resources of the Cornell Theory Center which receives support from the New York state and other federal agencies. In particular, we would like to acknowledge the support from the latest velocity cluster (V3) in CTC that significantly helped in accelerating the design simulator and reducing the total simulation time.

References

[1] M.C. Flemings, Solidification Processing, Mat. Sci Eng. Series, McGraw Hill Publ., 1974, pp. 214–262.
[2] W. Kurz, R. Fisher, Fundamentals of Solidification, third ed., Trans. Tech. Publ., 1981, pp. 117–132.
[3] S.D. Felicilli, J.C. Heinrich, D.R. Poirier, Numerical model for dendritic solidification of binary alloys, Numer. Heat Transfer B 23 (1993) 461–481.
[4] E. Mcbridge, J.C. Heinrich, D.R. Poirier, Numerical simulation of incompressible flow driven by density variations during phase change, Int. J. Numer. Meth. Fluids 31 (1999) 787–800.
[5] J.C. Heinrich, D.R. Poirier, Convection modelling in directional solidification, CR Acad. Sci. I – Mech. 332 (2004) 429–445.
[6] J. Ni, C. Beckermann, A volume-averaged two-phase model for transport phenomena during solidification, Metall. Trans. B 22 (1990) 349–361.
[7] C. Beckermann, Modeling of macrosegregation: application and future needs, Int. Math. Rev. 47 (2002) 243–261.
[8] F.P. Incropera, W.D. Bennon, A continuum model for momentum, heat and species transport in binary solid–liquid phase change systems – I. Model formulation, Int. J. Heat Mass Transfer 30 (1987) 2161–2170.
[9] P.J. Prescott, F.P. Incropera, Numerical simulation of a solidifying Pb–Sn alloy: the effects of cooling rate on thermosolutal convection and macrosegregation, Metall. Mater. Trans. B (22) (1991) 529–540.
[10] M.C. Schneider, C. Beckermann, Formation of macrosegregation by multicomponent thermosolutal convection during the solidification of steel, Metall. Mater. Trans. A 26A (1995) 2373–2388.
[11] J.P. Gu, C. Beckermann, Simulation of macrosegregation in a large steel ingot, Metall. Mater. Trans. A 30A (1999) 1357–1366.
[12] S.D. Felicelli, D.R. Poirier, J.C. Heinrich, Macrosegregation patterns in multicomponent alloys, J. Cryst. Growth 177 (1997) 145–161.
[13] S.D. Felicelli, J.C. Heinrich, D.R. Poirier, Finite element analysis of directional solidification of multicomponent alloys, Int. J. Numer. Meth. Fluids 27 (1998) 207–227.
[14] S.D. Felicelli, J.C. Heinrich, D.R. Poirier, Three dimensional simulations of freckles in binary alloys, J. Cryst. Growth 191 (1998) 879–888.
[15] J. Guo, C. Beckermann, Three dimensional simulations of freckle formation during binary alloy solidification: effect of mesh spacing, Numer. Heat Transfer A 44 (2003) 559–576.
[16] S.D. Felicelli, D.R. Poirier, J.C. Heinrich, Modeling freckle formation in three dimensions during solidification of multicomponent alloys, Metall. Mater. Trans. B 29B (1998) 847–854.
[17] C. Frueh, S.D. Felicelli, D.R. Poirier, Predicting freckle-defects in directionally solidified Pb–Sn alloys, Mater. Sci. Eng. A 328 (2002) 245–255.
[18] J.C. Ramirez, C. Beckermann, Evaluation of a Rayleigh-number-based freckle prediction criterion for Pb–Sn alloys and Ni-base superalloys, Metall. Mater. Trans. A 34A (2003) 1525–1536.
[19] S. Tin, T.M. Pollock, Predicting freckle formation in single crystal Ni-base superalloys, J. Mater. Sci. 39 (2004) 7199–7205.
[20] D.T.J. Hurle, Handbook of Crystal Growth – Growth Mechanisms and Dynamics, North-Holland, 1994.
[21] D.H. Kim, P.M. Adornato, R.A. Brown, Effect of vertical magnetic field on convection and segregation in vertical Bridgeman crystal growth, J. Cryst. Growth 89 (1988) 339–356.
[22] H. Ben Hadid, D. Henry, S. Kaddeche, Numerical study of convection in the horizontal Bridgeman configuration under the action of a constant magnetic field. 1. Two dimensional flow, J. Fluid Mech. 333 (1997) 23–56.
[23] H. Ben Hadid, D. Henry, Numerical study of convection in the horizontal Bridgeman configuration under the action of a constant magnetic field. 2. Three dimensional flow, J. Fluid Mech. 333 (1997) 57–83.
[24] P.J. Prescott, F.P. Incropera, Magnetically damped convection during solidification of a binary metal alloy, ASME J. Heat Transfer 115 (1993) 302–310.
[25] R. Sampath, N. Zabaras, Numerical study of convection in the directional solidification of a binary alloy driven by the combined action of buoyancy, surface tension and electromagnetic forces, J. Comput. Phys. 168 (2001) 384–411.
[26] R. Sampath, N. Zabaras, Inverse thermal design and control of solidification processes in the presence of a strong external magnetic field, Int. J. Numer. Meth. Eng. 50 (2001) 2489–2520.

[27] R. Sampath, N. Zabaras, A functional optimization approach to an inverse magneto-convection problem, Comput. Meth. Appl. Mech. Eng. 190 (15) (2001) 2063–2097.
[28] M. Gunzburger, E. Ozugurlu, J. Turner, H. Zhang, Controlling transport phenomena in the Czochralski crystal growth process, J. Cryst. Growth 234 (2002) 47–62.
[29] B. Ganapathysubramanian, N. Zabaras, Control of solidification of non-conducting materials using tailored magnetic fields, J. Cryst. Growth 276 (1/2) (2005) 299–316.
[30] B. Ganapathysubramanian, N. Zabaras, On the control of solidification using magnetic fields and magnetic field gradients, Int. J. Heat Mass Transfer 48 (2005) 4174–4189.
[31] W. Shyy, H.S. Udaykumar, M.M. Rao, R.W. Smith, Computational Fluid Dynamics with Moving Boundaries, first ed., Tailor and Francis, Washington, DC, 1996.
[32] J. Baumgartl, G. Müller, Calculation of the effects of magnetic field damping on fluid flow – comparison of magnetohydrodynamic models of different complexity, in: Proc. 8th European Symp. Mater. Fluid Science in Microgravity, ESA publ. no: SP. 333, 1992, pp. 161–164.
[33] S. Ganapathysubramanian, N. Zabaras, A continuum sensitivity method for finite thermo-inelastic deformations with applications to the design of hot forming processes, Int. J. Numer. Meth. Eng. 55 (2003) 1391–1437.
[34] D. Samanta, N. Zabaras, Modeling melt convection in alloy solidification using stabilized finite element techniques, Int. J. Numer. Meth. Eng. 64 (2005) 1769–1799.
[35] N. Zabaras, D. Samanta, A stabilized volume-averaging finite element method for flow in porous media and binary alloy solidification processes, Int. J. Numer. Meth. Eng. 60 (6) (2004) 1103–1138.